ARTICLE IN PRESS

Corrosion Science xxx (xxxx) xxxx

Contents lists available at ScienceDirect

Corrosion Science

journal homepage: www.elsevier.com/locate/corsci

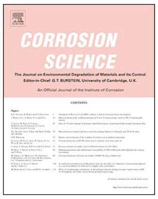

A high-resolution characterization of the initiation of stress corrosion crack in Alloy 690 in simulated pressurized water reactor primary water

Wenjun Kuang[a,b,*], Gary S. Was[b]

[a] Center for Advancing Materials Performance from the Nanoscale (CAMP-Nano), State Key Laboratory for Mechanical Behavior of Materials, Xi'an Jiaotong University, Xi'an 710049, PR China
[b] Department of Nuclear Engineering and Radiological Sciences, University of Michigan, Ann Arbor, MI 48109, United States

ARTICLE INFO

Keywords:
Alloy
STEM
Stress corrosion
Intergranular corrosion
Selective oxidation

ABSTRACT

Stress corrosion crack initiation of alloy 690 in simulated pressurized water reactor primary water was studied through high-resolution characterization of grain boundaries at different stages of the initiation process. It was found that a compact layer of Cr_2O_3 initially forms over a migrated grain boundary, driven by the diffusion of Cr. After the surface Cr_2O_3 is breached by straining, oxygen diffusion results in formation of a mixture of NiO and Cr_2O_3 along the grain boundary. The crack nucleates along either the previous grain boundary or the heavily oxidized migration zone when the boundary strength falls below the local stress.

1. Introduction

Nickel base alloy 690 is an important structural material in pressurized water reactors (PWR). This alloy is renowned for its high stress corrosion cracking (SCC) resistance [1–3] and no incidence of SCC has been reported since its initial application in nuclear power plants. Nevertheless, its SCC behavior is still highly of concern since SCC is the major issue for its predecessor-alloy 600. The current results from lab tests indicate that alloy 690 is not immune to either crack initiation [4–6] or propagation [7–12] in simulated PWR primary water regardless of the intergranular carbide density and cold work level. A better understanding of the SCC behavior of this alloy, especially the crack initiation, is much needed to assess its safety margin in the long-term operation of PWRs.

It is challenging to initiate SCC on alloy 690 and the research data on crack initiation of this alloy is still very limited. Arioka et al. [5,8] and Zhai et al. [13] reported that extensive creep cavities formed at grain boundaries in cold worked alloy 690 TT after long-term constant load tests in simulated PWR primary water, which are thought to be involved in crack initiation and growth processes as crack embryos. However, cavity formation is confined to cold worked alloy 690 with intergranular carbides and appears independent of the test environment. The recent microstructure characterization of SCC cracks after constant extension rate tensile (CERT) test by Kuang et al. [14] shows that no cavities formed near the crack tips of solution annealed (SA) alloy 690. Thus, creep cavitation induced cracking may be applicable only to cold worked alloy 690 with intergranular carbides, but not as a generic SCC mechanism for this alloy in high temperature water.

Compared to constant load or constant deflection test, dynamic straining test such as CERT is more efficient to initiate SCC cracks in alloy 690 in high temperature water, as reviewed by Moss et al. [15]. The cracks in alloy 690 after CERT tests in high temperature water should result from an environmentally-assisted cracking process because the same tests in inert environment did not produce cracks [6,16]. Based on the results from CERT tests, Moss et al. [15] proposed that the SCC initiation of alloy 690 occurs in three stages: 1) oxidation on the surface over the grain boundaries with the fast intergranular diffusion of Cr, 2) successive cycles of oxide film rupture and repair with the formation of Cr-depleted grain boundary migration zone, and 3) intergranular oxidation and rupture of oxides down the grain boundary. This model fits the existing SCC initiation data of alloy 690. A recent example is that of coherent twin boundaries in alloy 690 SA that does not undergo Cr depletion or boundary migration, and does not crack during CERT test in high temperature water. However, cold rolling damages the twin boundary structure and enhances Cr diffusion, grain boundary migration and cracking [17]. Grain boundary migration and intergranular oxidation were also observed beyond both stagnant and active SCC cracks of alloy 690 SA after CERT test in simulated PWR primary water [6,14].

Although the model proposed by Moss et al. [15] provides new

---

* Corresponding author at: Center for Advancing Materials Performance from the Nanoscale (CAMP-Nano), State Key Laboratory for Mechanical Behavior of Materials, Xi'an Jiaotong University, Xi'an 710049, PR China.
E-mail address: wjkuang66@gmail.com (W. Kuang).

https://doi.org/10.1016/j.corsci.2019.108243
Received 31 July 2019; Received in revised form 10 September 2019; Accepted 24 September 2019

Please cite this article as: Wenjun Kuang and Gary S. Was, Corrosion Science, https://doi.org/10.1016/j.corsci.2019.108243

insights into the SCC initiation of alloy 690 in simulated PWR primary water, it has not been fully supported by experimental results and still lacks details. The objective of this paper is to further substantiate the SCC initiation model by providing a more detailed picture of the initiation process. In this work, grain boundaries of alloy 690 at different stages of SCC initiation were sampled and analyzed following CERT tests in 360 °C hydrogenated water. In particular, the microstructure and elemental compositions of intergranular oxides and the grain boundary migration zone were examined. The results are discussed in relation to the main stages of SCC process.

2. Experimental

2.1. Material

The alloy 690 (57.6 wt.% Ni, 32.7% Cr, 8.64% Fe, 0.25% Mn, 0.315% Al, 0.08% Si and 0.02% C) was solution annealed (1100 °C/1 h) and water quenched. Tensile bars (20 mm in gauge length and 2 mm in diameter) were machined from a bar stock with lathe. The gauge section of the tensile bar was mechanically abraded to 4000 grit, electropolished (30 V/30 s) in a 10% (volume fraction) perchloric acid + 90% methanol solution at −30 °C and finally cleaned three times alternately with methanol and acetone. The sample contains a very low density of tiny carbides on the grain boundaries and shows no signs of grain boundary migration, as examined in a previous work [14].

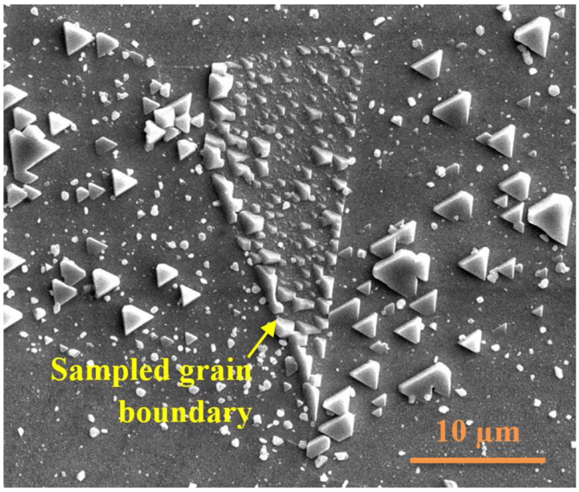

(a)

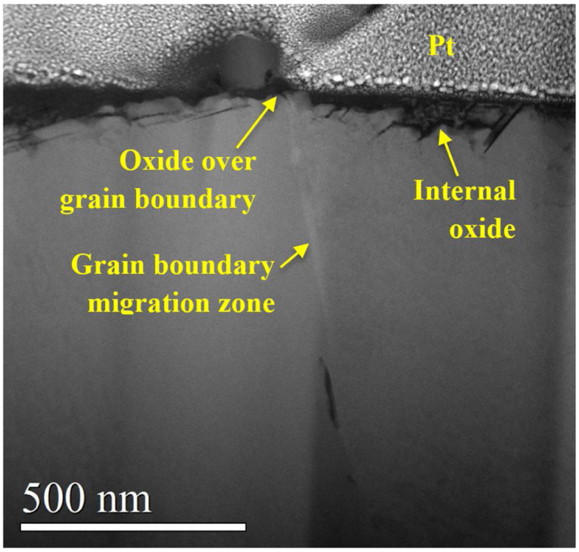

(b)

Fig. 1. (a) Scanning electron microscopy (SEM) image of grain boundary A from solution annealed alloy 690, strained to 1.78% at 1 × 10^{-8}/s in 360 °C high purity water containing 18 cm^3 (STP) H_2/kg H_2O, (b) STEM-HAADF image of the grain boundary cross section. The loading axis was aligned with the horizontal direction.

2.2. Apparatus and methodology

CERT test was conducted in 360 °C high purity water containing 18 cm^3 (STP) H_2/kg H_2O in a refreshed stainless-steel autoclave. As described in our previous work [4,18], once the environment parameters were stable, the samples were loaded to just below the yield point at a rate of 1.24 × 10^{-5} s^{-1} and then strained at 1 × 10^{-8} s^{-1}. The tensile bar was uniformly strained to 1.78% plastic strain after a total time of 564 h at temperature.

It is expected that there will exist a variation in the resistance to SCC initiation among different grain boundaries, resulting in different initiation times on different boundaries. Therefore, the grain boundaries should be at different stages of SCC initiation when the CERT test is stopped. To capture all the stages of SCC initiation, multiple grain boundaries were first examined using scanning electron microscopy (SEM) after the loading axis was aligned with the horizontal direction. Cross sections of the boundaries were made using focused ion beam (FIB) milling on a FEI Helios Nanolab 650. All the sampled grain boundaries are random high angle boundaries. The cross section was analyzed using a JEOL 2100 scanning transmission electron microscope (STEM) equipped with high angle annular dark-field (HAADF) and energy dispersive spectroscopy (EDS) detectors. High resolution images of intergranular oxides and the GB migration zone were taken in a JEOL 3100R05 STEM microscope equipped with HAADF and bright field (BF) detectors. Fast Fourier Transformation (FFT) was used to analyze the high-resolution images.

3. Results

Around 20 grain boundaries were sampled and categorized by the SCC initiation stages they were at. This paper will present four of them which are representative of the typical stages of SCC initiation. The analytical results from the four grain boundaries (A, B, C, D) will be presented in the order of increasing progression along the SCC initiation process.

3.1. Stage 1-oxidation above grain boundary A

Fig. 1a shows a SEM image of sampled grain boundary A. Each grain is covered by oxide particles with similar shape but different size. Our previous work [19] revealed that these particles are $NiFe_2O_4$ spinel and maintain epitaxy with the substrate. The grain boundary shows no sign of cracking. From the STEM-HAADF image of the cross section in Fig. 1b, there is a layer of compact oxide over the grain boundary which appears dark in the HAADF image. The thickness of the surface oxide is not uniform but decreases as the grain boundary is approached. Internal oxidation (selective formation of oxide in the matrix with the inward diffusion of oxygen) is observed in both grains. As reported earlier [19], internal oxides are composed mainly of chromia and develop preferentially along the most widely spaced lattice planes. The thin, brighter region along the grain boundary is the grain boundary migration zone, which extends up to ∼550 nm in depth. It appears brighter than the neighboring grain matrix in the HAADF image due to its higher Ni content. EDS line scans were performed across the migration zone as indicated on Fig. 2a. All the three scans (Fig. 2b–d) show that the migration zone is enriched in Ni and depleted in Cr. Ni content increases to approximately 75 at.% while Cr drops to ∼15 at.%. The microstructure of the oxide over the grain boundary was further examined through high resolution imaging. Fig. 3a and b show high resolution HAADF and BF images of the framed area on Fig. 2a. The left grain was tilted to the [110] zone axis so that the orientation relationship between the oxide and matrix can be better revealed. The oxide slightly penetrates along the grain boundary, as shown in Fig. 3a. The oxide over the grain boundary is amorphous as evidenced by the lack of lattice structure (Fig. 3b). The FFT of the left grain with the adjacent oxide (Fig. 3c) shows that the oxide has a corundum structure and maintains the following orientation relationship: corundum {006} // matrix {111}, corundum < 201 > // matrix < 110 > . The corundum was found to be Cr_2O_3 in previous work [19,20].

3.2. Stage 2-intergranular oxidation of grain boundaries B and C

Fig. 4a shows a SEM image of sampled grain boundary B. No sign of cracking can be found from the surface. The cross section (Fig. 4b) also shows oxide penetration into the grain matrix and a grain boundary migration zone as in grain boundary A. The grain boundary migration zone becomes thinner with increasing depth from the surface. The depth of the migration zone is up to ~560 nm. Moreover, there is a noticeable segment of intergranular oxide (~80 nm deep) above the grain boundary migration zone, confirming that grain boundary B is a step further along in the SCC initiation process than grain boundary A. Due to the unevenness of the FIB lamella, the area in the lower middle part of Fig. 4b looks brighter as it is thicker than the rest of the sample. Fig. 5 presents the results of EDS line scans. Line scan b is from the intergranular oxide to the migration zone along the grain boundary, and line scans c and d are across the grain boundary migration zone width. The profile from line scan b shows that the intergranular oxide is enriched in Cr and that the Cr content decreases as it moves into the migration zone while the Ni content increases rapidly (Fig. 5b). Fig. 5c and d show that the grain boundary migration zone is highly enriched in Ni and depleted in Cr. The Ni content from line scan c exceeds 80 at.%. The Cr enrichment from line scan c is a little higher than that from line scan d. Fig. 6a and b show the high resolution HAADF and BF images of the intergranular oxide with the right grain tilted to [110] zone axis. The sample was flipped over compared to Fig. 5a. The intergranular oxidation front is not fully oxidized as evidenced by the contrast between oxide and matrix. From Fig. 6a, the tip of oxidation front protrudes along the grain boundary. There are two sets of oxides

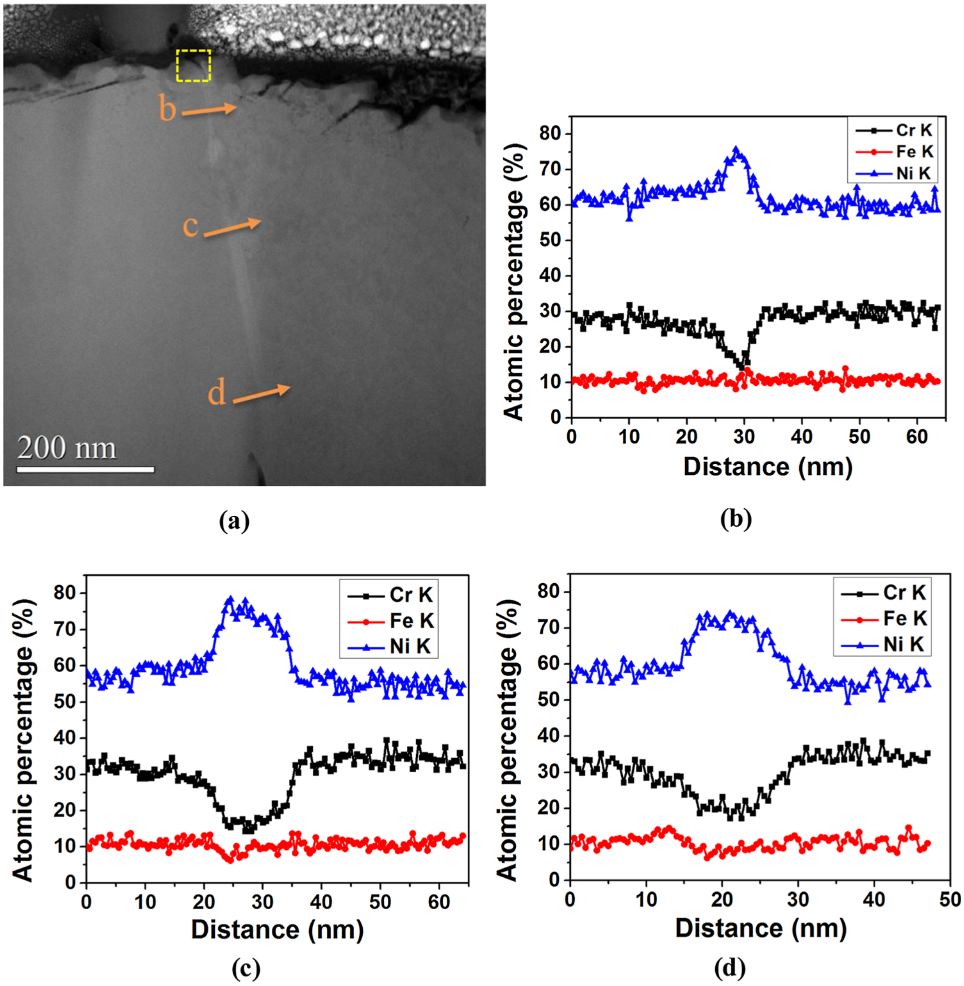

(a) (b)

(c) (d)

Fig. 2. (a) STEM-HAADF image of the cross section of grain boundary A from solution annealed alloy 690, strained to 1.78% at 1×10^{-8}/s in 360 °C high purity water containing 18 cm^3 (STP) H_2/kg H_2O and (b–d) EDS line profiles along lines b–d in (a).

growing from the neighboring grains. The FFT of the right grain with oxide shows that two types of oxide, NiO structure and corundum, formed with specific orientation relationships with the matrix (Fig. 6c). NiO structure is epitaxial with the matrix. The corundum has the same orientation relationship with the matrix as noted above although it is a different variant. All the variants were reported in [19]. As each oxide grain maintains a specific orientation relationship with the grain matrix into which it grows, the misorientation between the two sets of oxides inherits the original grain misorientation. Thus, the position of the original grain boundary can be determined based on the change of the orientation of the oxide as marked in Fig. 6b. The corundum should be Cr_2O_3 as it is Cr enriched (Fig. 5b). The NiO structure has also been found in a stagnant crack [20] and on crack walls [21] of alloy 690 which consists of NiO mixed with some Fe. Fig. 6d shows the enlarged image of the intergranular oxide tip framed in Fig. 6b. The oxide tip is amorphous and is outlined in Fig. 6d.

Deeper intergranular oxidation is observed on grain boundary C. Fig. 7a shows the SEM image of this boundary. The HAADF image of the cross section indicates that the intergranular oxidation extends to 230 nm below the surface. Internal oxidation and grain boundary migration are also observed. The grain boundary migration zone could not be easily identified as in previous grain boundaries because there is not much difference in contrast between this zone and the left grain. Nevertheless, the position of the migrated grain boundary is located based on the change of the grain lattice orientation and the contrast (Fig. 7b). The EDS line scan also confirms that the region beyond the intergranular oxide is enriched in Ni (~80%) and depleted in Cr (~15%) (Fig. 7d). The enlarged image of the framed area in Fig. 7b confirms that the migrated grain boundary separates two grains of different orientations (Fig. 7c). It is interesting to note that the oxide develops preferentially into the grain boundary migration zone, not along the migrated grain boundary (Fig. 7b and c). The oxide is also

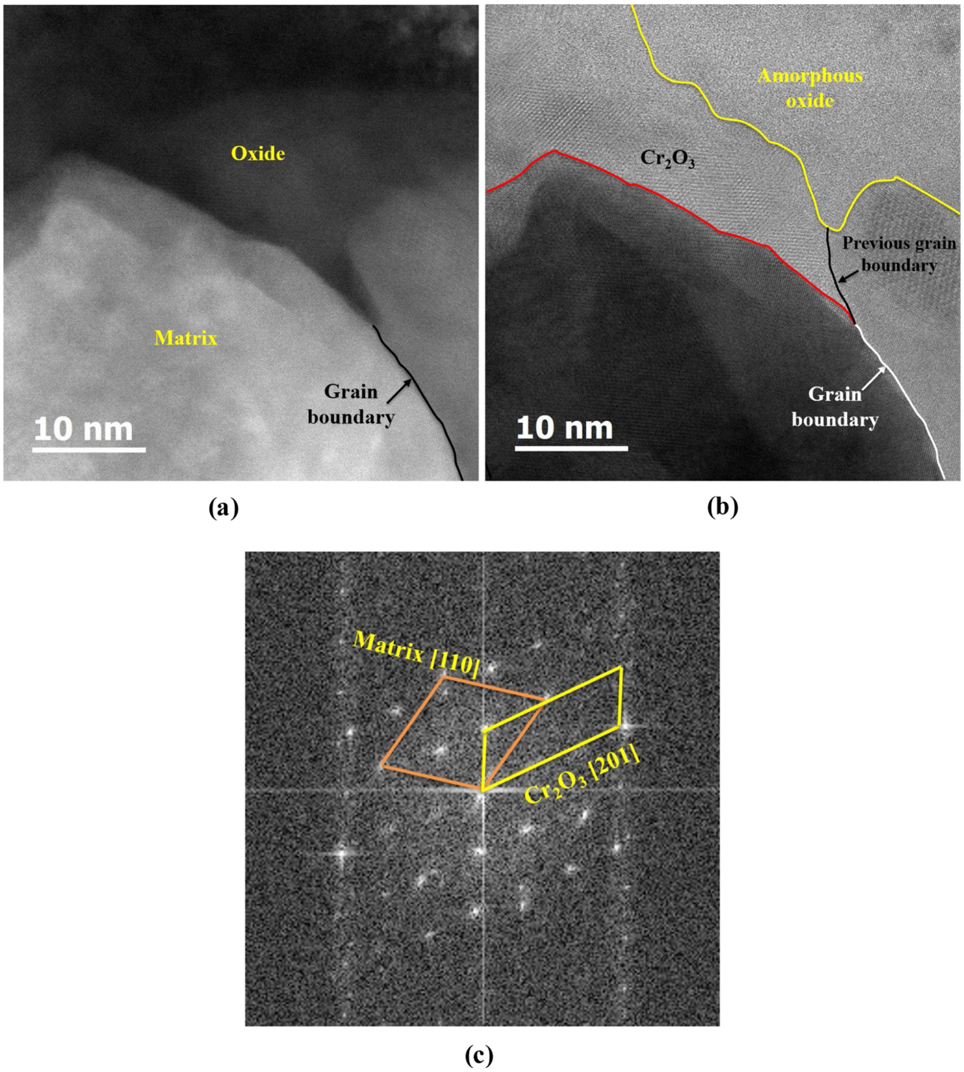

Fig. 3. Grain boundary A: (a) STEM-HAADF and (b) bright field (BF) images of the framed area on Fig. 2a with the left grain titled to [110] zone axis, (c) Fast Fourier Transformation (FFT) of the left grain with oxide showing corundum < 201 > // Matrix < 110 > .

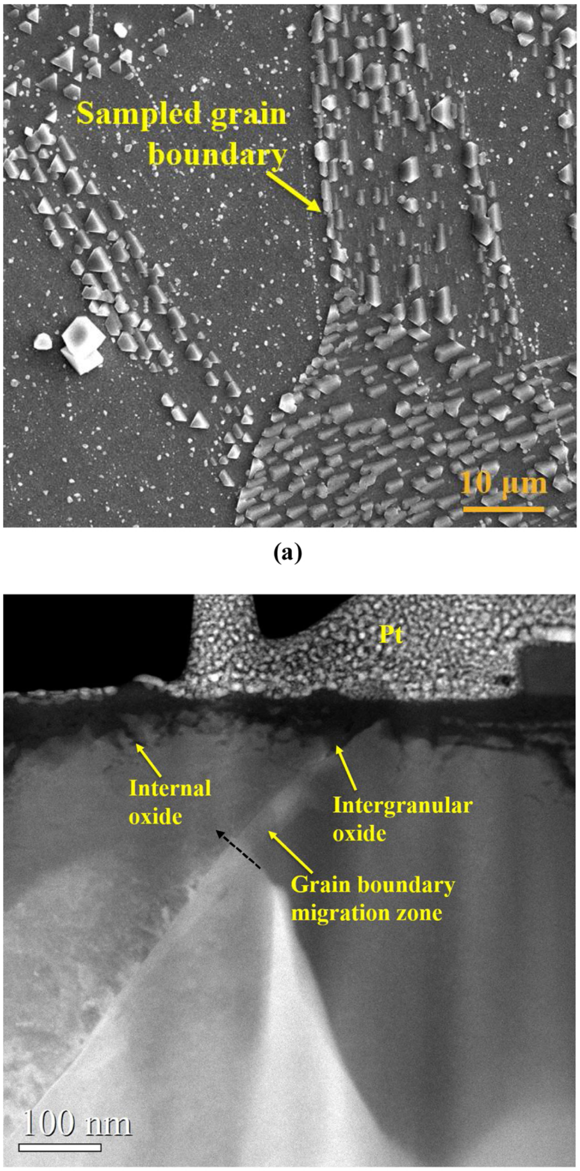

(a)

(b)

Fig. 4. (a) SEM image of grain boundary B from solution annealed alloy 690, strained to 1.78% at 1×10^{-8}/s in 360 °C high purity water containing 18 cm^3 (STP) H_2/kg H_2O, (b) STEM-HAADF image of the grain boundary cross section.

composed of NiO and Cr_2O_3.

3.3. Stage 3-crack nucleation of grain boundary D

Fig. 8 shows the SEM image of grain boundary D and the corresponding cross sections. There is no sign of cracking on the grain boundary from the plane view (Fig. 8a). The cross section shows extensive internal oxidation into both grains (Fig. 8b) and the depth of the internal oxidation region decreases as it approaches the grain boundary. The intergranular oxide is ~230 nm deep and beyond that there is a segment of grain boundary migration zone with a length of ~450 nm. Interestingly, the enlarged image of the area framed on Fig. 8b shows that there is a darker region within the intergranular oxide (Fig. 8c). This dark strip starts from the sample surface and extends into the intergranular oxide. A dark area in a HAADF image represents lower mass density, indicating that the dark area within the oxide should be thinner or porous. This dark strip is likely a crack embryo since the bond strength of a porous layer is low and it can readily develop into a crack with further straining. From Fig. 8c, the tip of the intergranular oxidation front is in the grain boundary migration zone. The elemental distribution of grain boundary migration zone was also checked with EDS line scans as indicated in Fig. 9a. The line scans show that the migration zone is notably enriched in Ni and depleted in Cr (Fig. 9b–d). The Ni content ranges from 75 at.% to 85 at.% and the Cr content is from 10 at.% to 20 at.%. The elemental composition is quite constant across the migration zone width and the compositions in the neighboring grains were unaffected, consistent with previous work [14]. The microstructure of intergranular oxide was further investigated with the right grain tilted to the [110] zone axis (Fig. 10). The FFT of the right grain indicates that it is composed of NiO and Cr_2O_3 that maintain the same specific orientation relationships with the matrix as mentioned earlier. The previous grain boundary location was determined based on the change of orientation of the oxide. The enlarged image in frame b on Fig. 10a shows that the intergranular oxide develops into both grains and the darker crack embryo follows the previous grain boundary (Fig. 10b). Figs. 10c and 10d show high resolution BF images of framed areas b and c, respectively, in Fig. 10a. The oxide against the right grain was confirmed to consist of NiO and Cr_2O_3 via FFT. NiO tends to segregate near the previous grain boundary while Cr_2O_3 lies against the matrix (Fig. 10c). From Fig. 10d, Cr_2O_3 dominates near the tip of the intergranular oxide and the oxide at the tip is amorphous. Consistent oxide structure has also been found in a stagnant crack as described in [14].

4. Discussion

All three stages of SCC initiation in alloy 690 (oxidation over the grain boundary, oxidation down the grain boundary, and crack nucleation) are captured in samples A–D. In the following, each stage will be discussed in the context of the samples studied.

4.1. Oxidation over the grain boundary

Alloy 690 tends to form a thin compact oxide layer over grain boundary in hydrogenated high temperature water before crack initiation occurs (Fig. 1). The oxide is predominantly chromia (Fig. 3) and is supported by the outward diffusion of Cr along the grain boundary as evidenced by a Cr depleted migration zone formed beneath the surface oxide layer (Fig. 2). Olszta et al. [22] and Moss et al. [23] also reported that a compact layer of Cr_2O_3 forms over grain boundary on unstressed alloy 690 coupons, and that the grain boundary migrates beneath the oxide layer after exposure in hydrogenated high temperature water. The outward diffusing Cr not only supports the formation of Cr_2O_3 above the grain boundary, but also diffuses laterally and is incorporated into the internal oxide that penetrates the grain matrix. The closer the internal oxide is to the grain boundary, the more protective it is, which is why the depth of the internal oxide layer decreases as it approaches the grain boundary (Fig. 1b). Calvarin et al. [24] reported a similar oxide morphology over the grain boundary of Ni-20Cr foils after exposure to air between 500 and 900 °C. Kim et al. [25,26] found that a protective Cr-rich oxide layer forms near random grain boundaries while a thicker, Fe-rich oxide layer forms in the intra-grain region on austenitic stainless steel after exposure to 700 °C steam. It should be noted here that the grain boundary structure plays an important role in the oxidation process. There is no protective, compact oxide layer above the coherent twin boundaries of alloy 690 [17]. Instead, a thin

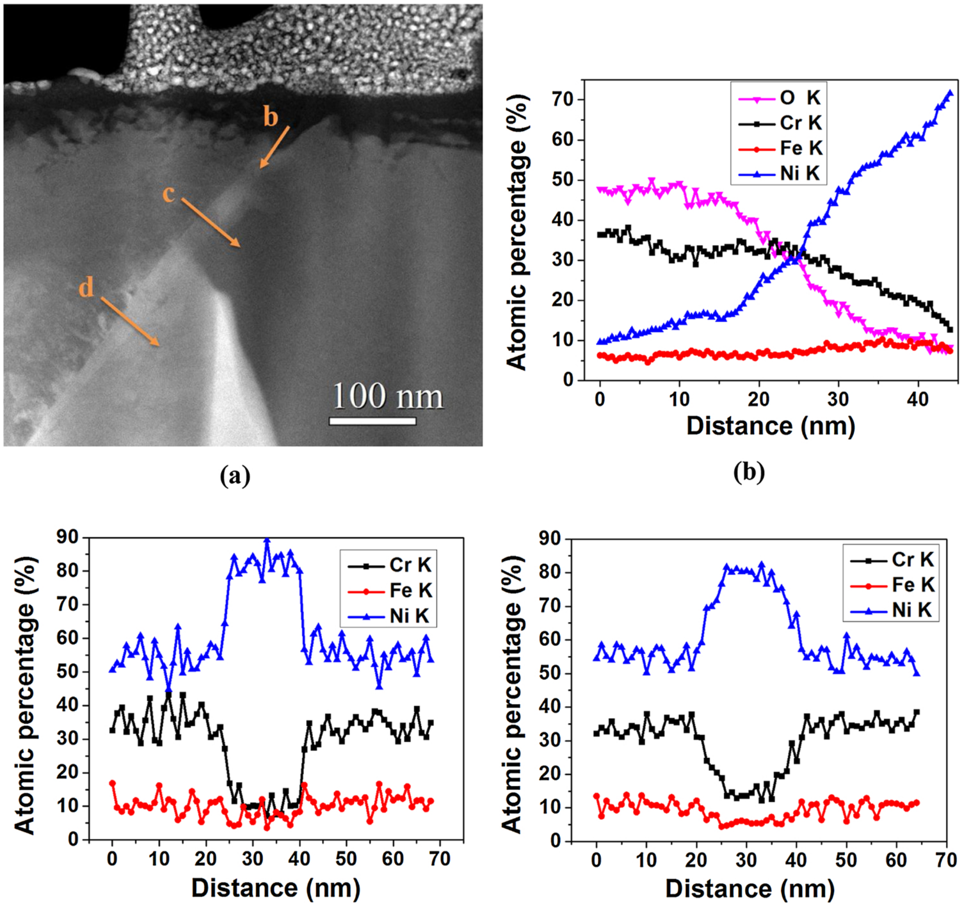

(a) (b)

(c) (d)

Fig. 5. (a) STEM-HAADF image of the cross section of grain boundary B from solution annealed alloy 690, strained to 1.78% at 1 × 10^{-8}/s in 360 °C high purity water containing 18 cm^3 (STP) H_2/kg H_2O and (b–d) EDS line profiles along lines b–d in (a).

layer of discrete Cr_2O_3 platelets forms along the twin boundary. When the twin boundary structure is damaged by cold rolling, the oxide morphology formed above it is the same as that above a random high angle grain boundary.

The oxide over the grain boundary is different from the internal oxide penetrating the grain matrix in both structure and its formation process. The oxide over the grain boundary is predominantly Cr_2O_3 with some amorphous regions (Fig. 3). As mentioned above, the outward diffusion of Cr is an important step during the oxidation process which induces grain boundary migration. As for the internal oxide in the matrix, it is a mixture of $(Fe,Cr,Ni)_3O_4$ spinel and Cr_2O_3 where the Cr_2O_3 develops in the form of filament along the most widely spaced lattice planes of the matrix [19]. The basic difference between these two oxidation processes is the source of Cr. The grain boundary is a fast diffusion path for Cr that supports the formation of a compact, protective oxide layer over the grain boundary. However, a compact Cr_2O_3 layer cannot form in the matrix due to the limitation of lattice diffusion supplying Cr to the surface [27]. Thus, the internal oxide is not protective, and oxygen can continuously diffuse inwards.

The ability to form a compact Cr_2O_3 layer over the grain boundary on alloy 690 leads to its higher resistance to intergranular oxidation than alloy 600. However, alloy 690 is not immune to intergranular oxidation under dynamic straining.

4.2. Penetrative oxidation down the grain boundary

Intergranular oxidation has been reported to occur on unstressed alloy 600 coupons in high temperature hydrogenated water [28,29] and steam [30,31], and to extend beyond the crack tip [32–35]. Although alloy 690 tends to form protective oxide over the grain boundary, when the protective oxide layer is breached by dynamic straining and unable to recover, the Cr depleted grain boundary is oxidized due to the inward diffusion of oxygen [15]. The intergranular oxide is a mixture of NiO structure oxide and Cr_2O_3. The formation of NiO is mainly due to the locally high Ni content (Figs. 5 and 9) and a high electrochemical potential that promotes the thermodynamic stability of this oxide. The dissolved hydrogen concentration (18 cc H_2/kg H_2O) is below the value corresponding to the Ni/NiO transition (25 cc H_2/kg H_2O) [36], making its formation thermodynamically possible. Formation of NiO on the grain matrix has also been reported in oxygenated water [37,38]. The intergranular oxide can grow into both adjacent grains, as shown on grain boundary B (Fig. 6). In this case, two sets of oxides develop along the original grain boundary that maintain specific orientation relationships with the neighboring grains. The propagation of the oxidation front down the grain boundary (Fig. 6a) is supported by the higher intergranular diffusion rate of oxygen compared to lattice diffusion. Previous work [14] has shown that the intergranular oxide beyond a stagnant crack consists of NiO in the crack center and a compact layer of Cr_2O_3 between NiO and matrix. Oxidation can also occur preferentially in the grain boundary migration zone where the Cr content is low, as shown on grain boundary C (Fig. 7). The oxidation rate is higher than the internal oxidation rate of matrix (Fig. 7b), and the oxide is not compact as it is a mixture of NiO structure oxide, Cr_2O_3 and matrix. Similar oxide preferentially formed in the grain boundary migration zone has also been observed beyond an active crack of the same heat of alloy 690 [14].

It is interesting to note that the intergranular oxide grows into both grains on grain boundary B while it forms preferentially in the grain migration zone on boundary C. It seems that some grain boundaries show very narrow or no migration zone near the sample surface, such as grain boundary A. For those grain boundaries, when the surface oxide layer is breached, the oxygen diffusing preferentially along the boundary reacts with both grains, as shown in grain boundaries A and B (Figs. 3a and 6 a). Only when oxygen reaches the migration zone does it begin to react preferentially with the Cr-depleted zone, as shown in grain boundaries C and D (Figs. 7b and 8 c). The oxide formed along the grain boundary (Fig. 6a) looks more compact than that formed in the grain boundary migration zone (Fig. 7b). The compactness of oxide may be related to the efficiency of Cr diffusion. He et al. [39] also suggested that the efficiency of Cr transport along GBs and the protectiveness of inner oxides are critical to the local SCC susceptibility. It has been

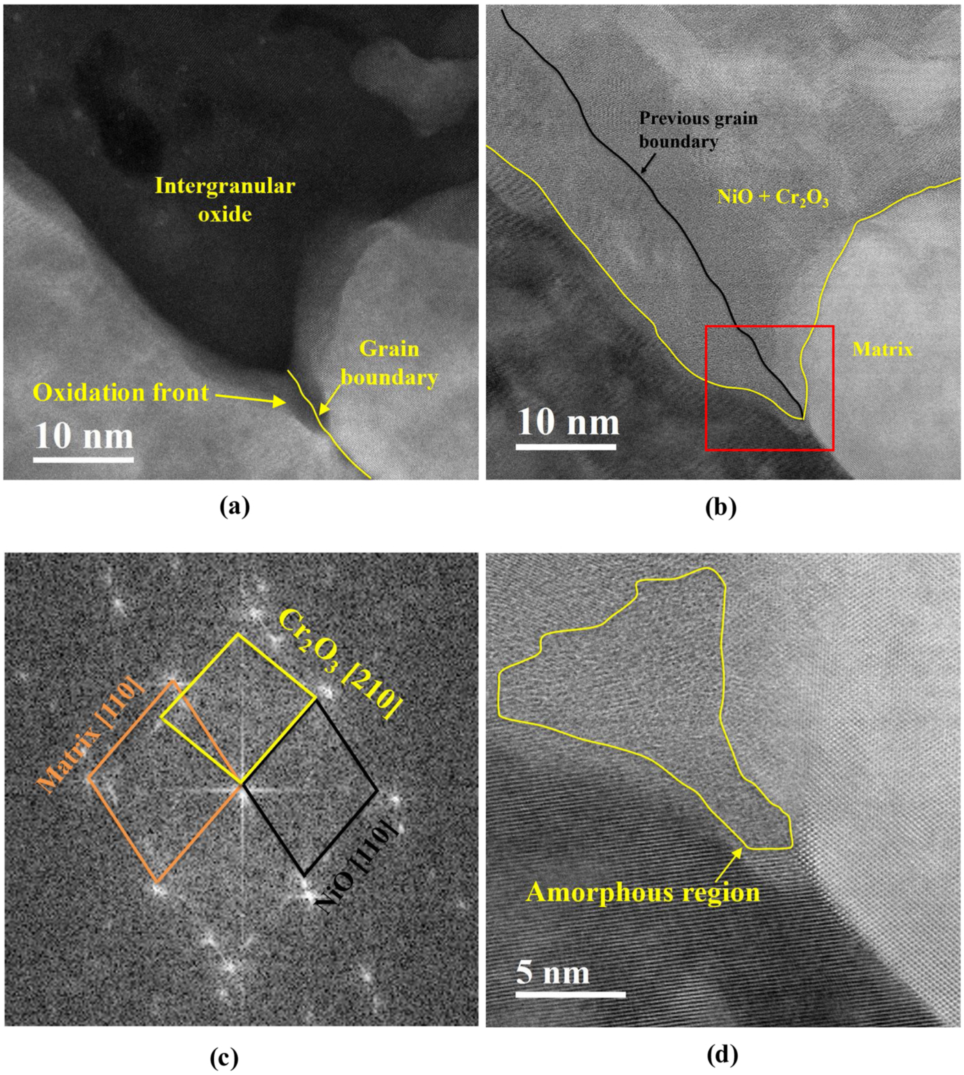

Fig. 6. Grain boundary B: (a–b) STEM-HAADF and bright field (BF)images of the cross section of the boundary with the right grain titled to [110] axis, (c) Fast Fourier Transformation (FFT) of the right grain with oxide, and (d) high resolution BF image taken from the selected areas on (b).

reported in our previous work [14] that the outward diffusion of Cr in the migration zone is along the grain boundary, not by lattice diffusion. During the oxidation of the grain boundary migration zone, only oxygen diffuses into the Cr depleted migration zone and a non-compact oxide forms, as shown in Fig. 7b. A similar non-compact oxide has been observed in the grain boundary migration zone beyond an active crack in the same heat of alloy 690 [14]. For oxidation along the unmigrated grain boundary, inward diffusion of oxygen and outward diffusion of Cr must occur simultaneously, promoting the formation of a more compact intergranular oxide, as shown in Figs. 3a and 6 a.

4.3. Crack nucleation

It has been reported that the grain boundary strength of alloy 600 degrades significantly after exposure in PWR primary water [40–43]. The decrease in grain boundary strength is closely related to the formation of intergranular oxide. Similarly, the grain boundary strength would also decrease in alloy 690 when intergranular oxidation occurs during dynamic straining. Cracking will occur when the grain boundary strength drops below the applied stress. Fig. 10 shows that the crack embryo nucleates within the porous, intergranular oxide along the previous grain boundary. However, Fujii et al. [41] and Dugdale et al. [40] reported that the crack nucleated along the oxide/matrix interface on alloy 600 when testing single grain boundaries from samples

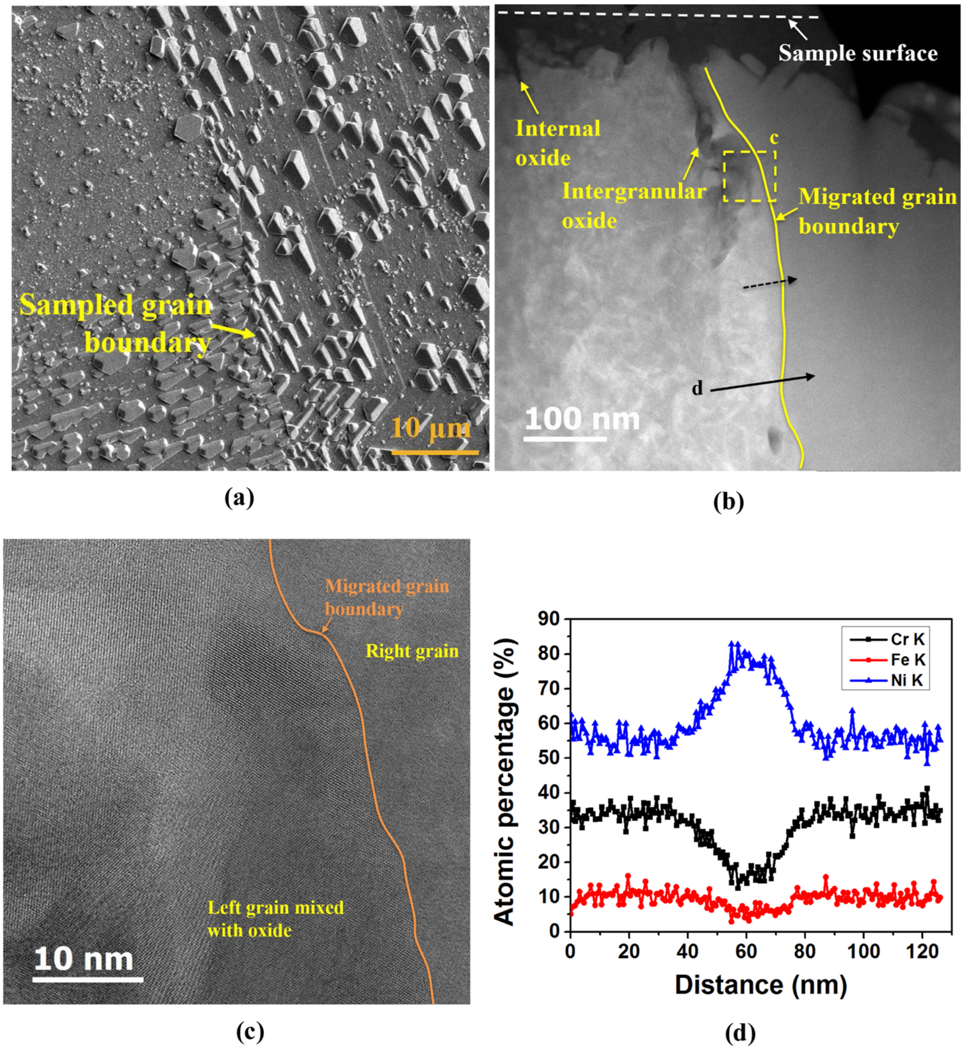

Fig. 7. (a) SEM image of grain boundary C from solution annealed alloy 690, strained to 1.78% at 1×10^{-8}/s in 360 °C high purity water containing 18 cm^3 (STP) H_2/kg H_2O, (b) STEM-HAADF image of the grain boundary cross section, (c) enlarged BF image of the framed area in (b) and (d) EDS line profile along line d in (b).

oxidized in PWR primary water. Dohr et al. [43] conducted a similar test and found that the grain boundary of alloy 600 fractured along the oxide/matrix interface while fracture in 304 stainless steel occurred in the intergranular oxide. However, Stratulat et al. [42] found that the crack was contained entirely within the intergranular oxide when the notched cantilevers milled at individual grain boundaries on alloy 600 after exposure to simulated PWR environment were bent. More recently, Couvant [44] reported that the crack could initiate either within the intergranular oxide or at the metal/oxide interface on alloy 600. In this work, the intergranular oxide in grain boundary D is composed of two sets of oxides which maintain specific orientation relationships with the respective, neighboring grains. The two sets of oxides are not orientationally related with each other and the interface between them should be disordered and have lower bond strength than the oxide/matrix interface. So, the crack nucleated along the interface between the two sets of oxides (Fig. 10b). However, when oxygen reaches the grain boundary migration zone and a non-compact oxide forms (as in grain boundary C), the crack will form in the highly oxidized region. We have also reported that the crack propagated along the oxidized grain boundary migration zone for both transformed twin boundaries [17] and random high angle grain boundaries [14]. So, the crack could nucleate along either the oxide interface which follows the previous grain boundary or the oxidized grain boundary migration zone, depending on the structure of the intergranular oxide.

Thus far, there is no well-established cracking criteria for the oxidized grain boundary. No consensus has been reached as to the threshold stresses for cracking from the different micro mechanical tests on individual grain boundaries in alloy 600 [40,41,43]. In the 'local'

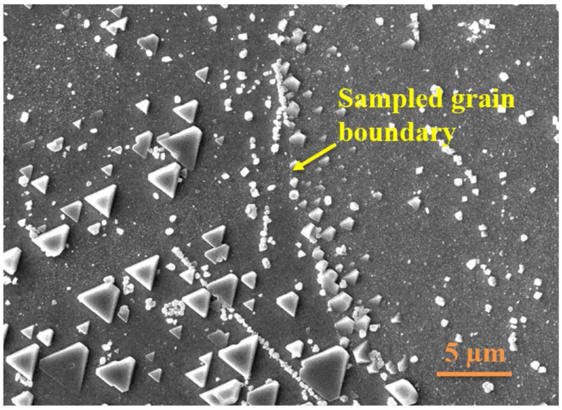

(a)

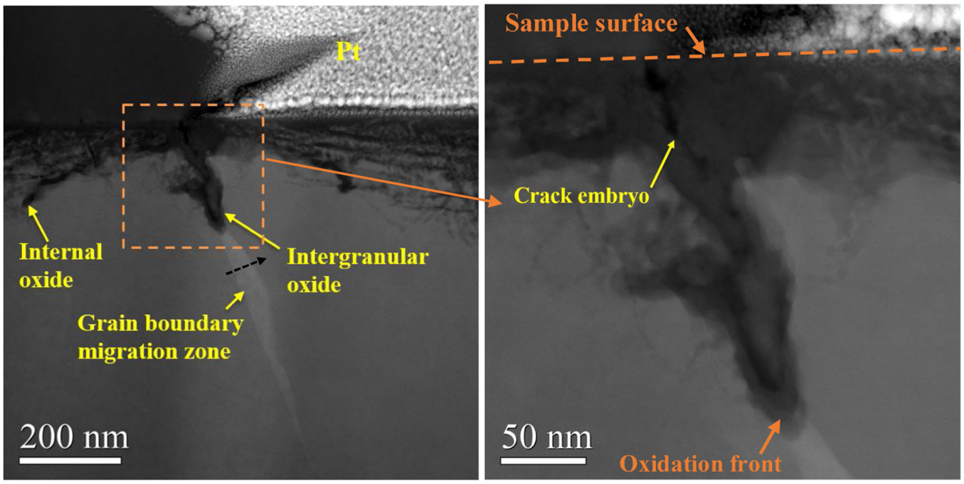

(b) (c)

Fig. 8. (a) SEM image of grain boundary D from solution annealed alloy 690, strained to 1.78% at 1×10^{-8}/s in 360 °C high purity water containing 18 cm^3 (STP) H_2/kg H_2O, (b) STEM-HAADF image of the grain boundary cross section, (c) enlarged image of the framed area in (b).

model developed by Couvant et al. [44], the threshold stress to fracture an oxidized grain boundary of alloy 600 was related to a critical intergranular oxidation depth. The grain boundary structure should have a major influence on the resistance to intergranular cracking. On one hand, the grain boundary structure affects the structure of the intergranular oxide. We [17] have reported that the coherent twin boundaries of alloy 690 tend to form intergranular oxides but is still very resistant to cracking. Our further results show that the penetrative intergranular oxide is composed of chromia, which maintains a specific orientation relationship with one grain (not presented here) [45], similar to the internal chromia filament formed in the grain matrix [19]. Here it is shown that the oxide formed along random high angle boundaries is composed of NiO and Cr_2O_3 with a disordered interface between them (Figs. 6 and 10). The difference in intergranular oxide structure should partly account for the difference in fracture stress. The higher cracking resistance of the twin boundary should be related to the special intergranular oxide structure. On the other hand, the grain boundary structure also dictates the compatibility between the slip systems of the neighboring grains, which determines the local stress and strain states near the grain boundary during loading. West and Was [46] have reported that slip discontinuity promotes intergranular cracking in irradiated stainless steel. Similarly, it has been reported that the strain heterogeneity near grain boundary strongly enhanced the intergranular oxidation rate of alloy 82 [47]. McMurtrey et al. [48] studied the mechanism of dislocation channel-induced irradiation assisted SCC initiation in austenitic stainless steel and found that discontinuous channel at the intersection with grain boundaries can raise high local stress and increases susceptibility to crack initiation accordingly. More work is still needed to correlate the grain boundary structure with the susceptibility to cracking in alloy 690.

This work presents detailed high-resolution microstructure analysis on individual grain boundaries at different SCC initiation stages from a single well controlled test, allowing the complete SCC initiation process to be elucidated by linkage between stages. The three SCC initiation stages of alloy 690 are shown schematically in Fig. 11. In the initial stage, Cr diffuses out along the grain boundary and forms a compact layer of Cr_2O_3 on the surface (Fig. 11a). The diffusion of Cr up the grain boundary induces grain boundary migration. Dynamic straining cracks

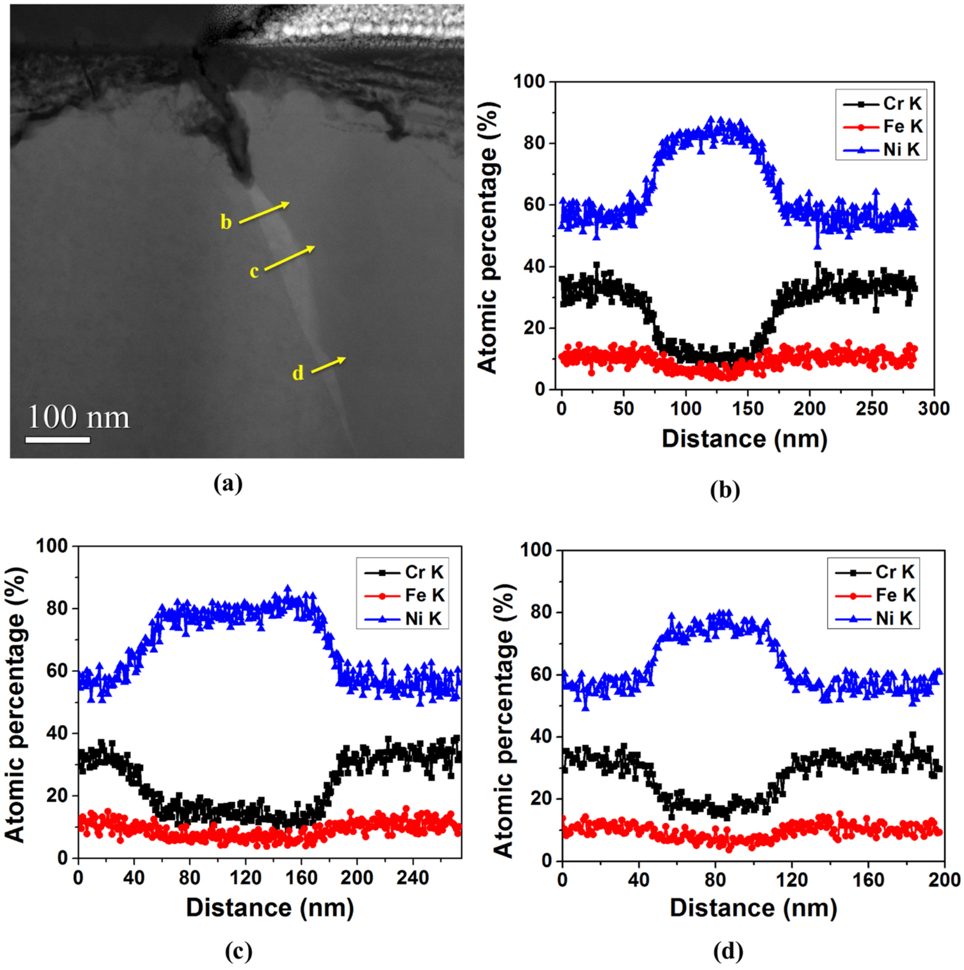

(a) (b) (c) (d)

Fig. 9. (a) STEM-HAADF image of the cross section of grain boundary D from solution annealed alloy 690, strained to 1.78% at 1×10^{-8}/s in 360 °C high purity water containing 18 cm^3 (STP) H_2/kg H_2O and (b–d) EDS line profiles along lines b–d in (a).

the surface Cr_2O_3 layer, resulting in oxygen diffusion down the grain boundary and formation of intergranular oxide (Fig. 11b). The grain boundary strength decreases with increasing intergranular oxide formation. In the last stage, the applied stress causes a crack to nucleate within the intergranular oxide when the boundary strength drops below the applied stress and oxygen continues to diffuse into the migration zone (Fig. 11c). The crack will actively grow along the oxidized migration zone if a diffusion barrier layer cannot form at the crack tip.

5. Conclusions

Grain boundaries of alloy 690 at different stages of stress corrosion crack (SCC) initiation were analyzed following a constant extension rate tensile (CERT) test in simulated PWR primary water. At the initial stage, a compact layer of Cr_2O_3 forms on the surface over the grain boundary and is accompanied by the migration of grain boundary due to the diffusion of Cr to the surface. The oxide layer is thinnest above the grain boundary, reflecting its compact, protective nature. Dynamic straining fractures the surface oxide allowing the formation of NiO and Cr_2O_3 down the grain boundary or into the grain boundary migration zone. NiO is epitaxial with the matrix and Cr_2O_3 maintains a specific orientation relationship with the matrix: Cr_2O_3 $\{006\}$ // matrix $\{111\}$, Cr_2O_3 $< 210 >$ // matrix $< 110 >$. As the oxidation proceeds, crack nucleates within the oxide, either along the original grain boundary or in the migration zone. The grain boundary structure plays a dominant role in the resistance of intergranular SCC as it affects the structure of the intergranular oxide as well as the mechanical process during deformation. The different crack initiation stages from different grain boundaries can be linked to reveal the full process of SCC initiation in alloy 690 in simulated PWR water.

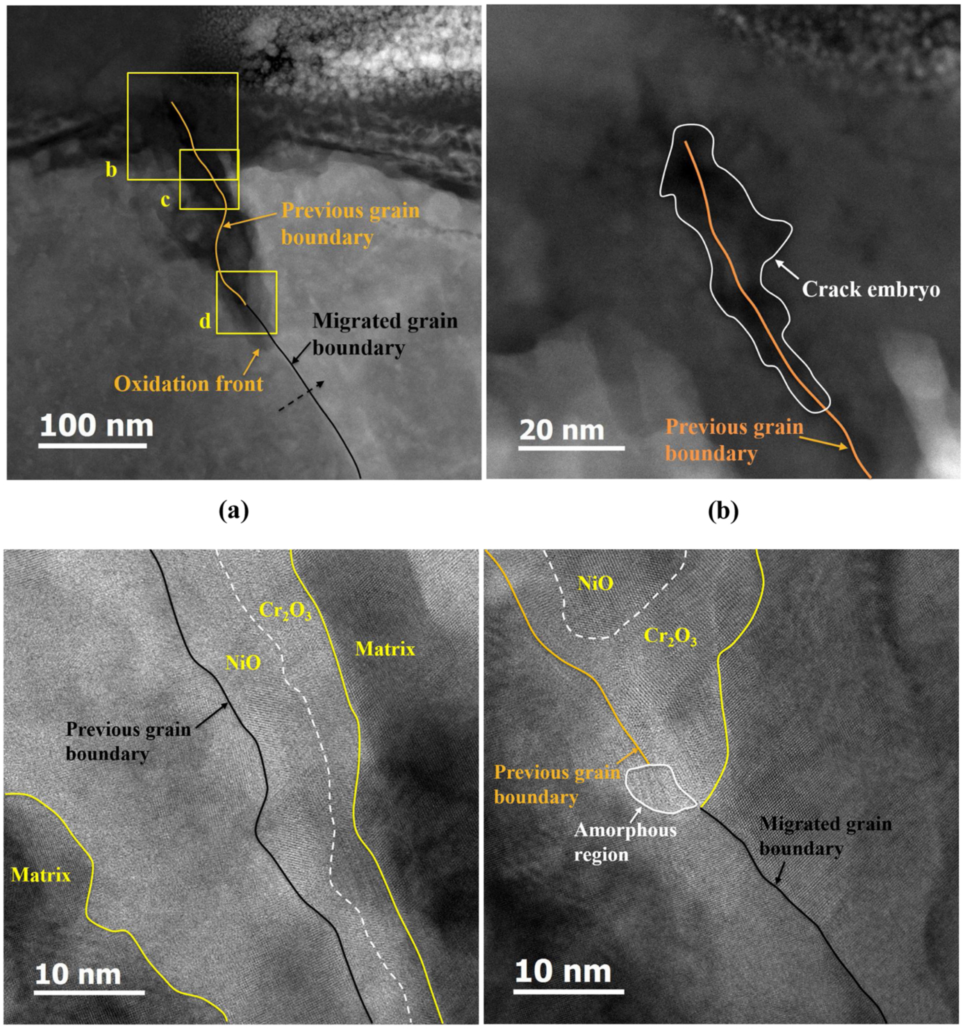

(a) (b)

(c) (d)

Fig. 10. (a) STEM-HAADF of the cross section of grain boundary D with the right grain titled to [110] axis, (b) enlarged HAADF image from frame b on (a), (c–d) high resolution BF images from selected areas on (a).

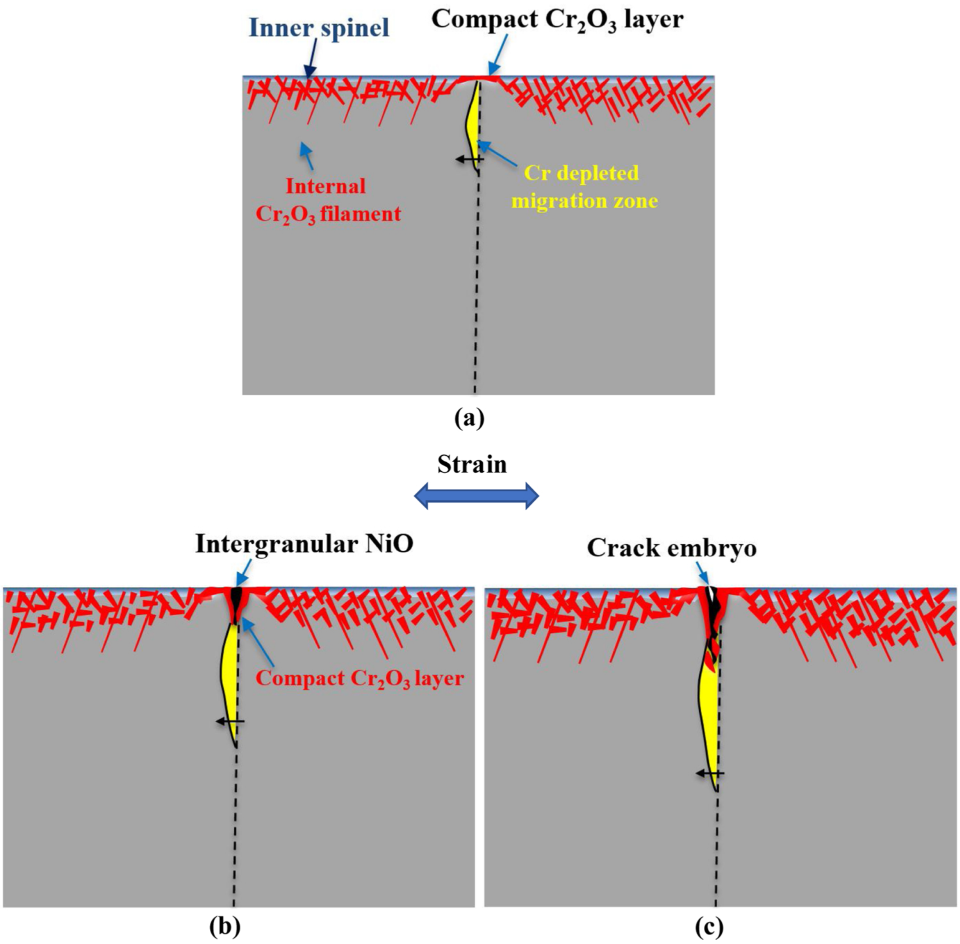

Fig. 11. Schematics of the SCC initiation stages of alloy 690 in simulated PWR primary environment under dynamic straining, (a) formation of compact Cr_2O_3 above the migrated grain boundary, (b) intergranular oxidation as the surface Cr_2O_3 is breached by straining and (c) crack nucleation within the intergranular oxide as the oxidation proceeds along the migration zone.

Declaration of Competing Interest

There is no conflict of interest.

Data availability

The raw/processed data required to reproduce these findings cannot be shared at this time as the data also forms part of an ongoing study.

Acknowledgements

The authors gratefully acknowledge financial support through the DOE I-NERI program contract 2011-01-K. The authors would like to thank Young Suk Kim and Sung Soo Kim from Korea Atomic Energy Research Institute for providing the materials for this study, and Alex Flick from the University of Michigan for his assistance with preparation of the high temperature autoclave systems in the Irradiated Materials Testing Laboratory.

References

[1] K. Smith, A. Klein, P. Saint-Paul, J. Blanchet, Inconel 690: a material with improved corrosion resistance for PWR steam generator tubes, Proceedings of the Second International Symposium on Environmental Degradation of Materials in Nuclear Power Systems-water Reactors, American Nuclear Society, Monterey, California, 1985.

[2] K. Norring, J. Engstrom, P. Norberg, Intergranular stress corrosion cracking in steam generator tubing. Testing of alloy 690 and alloy 600 tubes, Proc. 3rd Int. Symp. Environmental Degradation of Materials in Nuclear Power Systems — Water Reactors, Traverse City, Michigan, 1987.

[3] J.J. Kai, C.H. Tsai, G.P. Yu, The IGSCC, sensitization, and microstructure study of Alloys 600 and 690, Nucl. Eng. Des. 144 (1993) 449–457.

[4] W. Kuang, G.S. Was, The effects of grain boundary carbide density and strain rate on the stress corrosion cracking behavior of cold rolled Alloy 690, Corros. Sci. 97 (2015) 107–114.

[5] K. Arioka, T. Terachi, Degradation of Alloy 690 after relatively short times, Corrosion 72 (2016) 1252–1268.

[6] T. Moss, G.S. Was, Accelerated stress corrosion crack initiation of alloys 600 and 690 in hydrogenated supercritical water, Metall. Mater. Trans. A (2017) 1–16.

[7] M.B. Toloczko, M.J. Olszta, S.M. Bruemmer, One dimentional cold rolling effects on stress corrosion crack growth in Alloy 690 tubing and plate materials, 15th Int. Conf. on Environmental Degradation of Materials in Nuclear Power Systems-Water Reactors, Colorado Springs, Colorado, USA, 2011.

[8] K. Arioka, T. Yamada, T. Miyamoto, T. Terachi, Dependence of stress corrosion cracking of Alloy 690 on temperature, cold work, and carbide precipitation—role of diffusion of vacancies at crack tips, Corrosion 67 (2011) 035006-1-035006-18.

[9] D.J. Paraventi, W.C. Moshier, Primary water stress corrosion crack growth in cold worked Alloy 690 plate, 16th International Conference on Environmental Degradation of Materials in Nuclear Power Systems-Water Reactors, Asheville, North Carolina, USA, 2013.

[10] P.L. Andresen, M.M. Morra, K. Ahluwalia, Effect of deformation temperature, orientation and carbides on SCC of Alloy 690, 16th International Conference on Environmental Degradation of Materials in Nuclear Power Systems-Water Reactors, Asheville, North Carolina, USA, 2013.

[11] M.B. Toloczko, S.M. Bruemmer, Cack growth response of Alloy 690 in simulated PWR primary water, 14th Int. Conf. on Environmental Degradation of Materials in Nuclear Power Systems, Virginia Beach, VA, 2009.

[12] P.L. Andresen, M.M. Morra, A. Ahluwalia, J. Wilson, Effect of deformation and orientation on SCC of Alloy 690, 14th Int. Conf. on Environmental Degradation of Materials in Nuclear Power Systems, Virginia Beach, VA, 2009.

[13] Z. Zhai, M. Toloczko, K. Kruska, S. Bruemmer, Precursor evolution and stress corrosion cracking initiation of cold-worked alloy 690 in simulated pressurized water reactor primary water, Corrosion 73 (2017) 1224–1236.

[14] W. Kuang, M. Song, G.S. Was, Insights into the stress corrosion cracking of solution annealed Alloy 690 in simulated pressurized water reactor primary water under dynamic straining, Acta Mater. 151 (2018) 321–333.

[15] T. Moss, W. Kuang, G.S. Was, Stress corrosion crack initiation in Alloy 690 in high temperature water, Curr. Opin. Solid State Mater. Sci. 22 (2018) 16–25.

[16] J.M. Boursier, F. Vaillant, P. Saulay, Y. Brechet, G. Zacharie, Effect of the strain rate on the stress corrosion cracking in High temperature primary Water : comparison between the Alloys 690 and 600, 11th Int. Conf. Environmental Degradation of Materials in Nuclear Systems, Stevenson, WA, 2003.

[17] W. Kuang, G.S. Was, C. Miller, M. Kaufman, T. Alam, B. Gwalani, R. Banerjee, The effect of cold rolling on grain boundary structure and stress corrosion cracking susceptibility of twins in alloy 690 in simulated PWR primary water environment, Corros. Sci. 130 (2018) 126–137.

[18] W. Kuang, G.S. Was, The effects of strain rate and carbon concentration on the dynamic strain aging of cold rolled Ni-based alloy in high temperature water, Scripta Mater. 107 (2015) 107–110.

[19] W. Kuang, M. Song, P. Wang, G.S. Was, The oxidation of Alloy 690 in simulated pressurized water reactor primary water, Corros. Sci. 126 (2017) 227–237.

[20] W. Kuang, M. Song, C.M. Parish, G.S. Was, Microstructural study on the stress corrosion cracking of Alloy 690 in simulated pressurized water reactor primary environment, in: J.H. Jackson, D. Paraventi, M. Wright (Eds.), Proceedings of the 18th International Conference on Environmental Degradation of Materials in Nuclear Power Systems – Water Reactors, vol. 1, Springer International Publishing: Cham., 2018, pp. 535–545.

[21] M.J. Olszta, D.K. Schreiber, L.E. Thomas, S.M. Bruemmer, Penetrative internal oxidation from alloy 690 surface and stress corrosion crack walls during exposure to PWR primary water, 15th Int. Conf. on Environmental Degradation of Materials in Nuclear Power Systems-Water Reactors, Colorado Springs, Colorado, USA, 2011.

[22] M.J. Olszta, D.K. Schreiber, M.B. Toloczko, S.M. Bruemmer, Alloy 690 surface nanostructures during exposure to PWR primary water and potential influence on stress corrosion crack initiation, The 16th International Conference on Environmental Degradation of Materials in Nuclear Power Systems-Water Reactors, Asheville, North Carolina, USA, 2013.

[23] T. Moss, G. Cao, G.S. Was, Oxidation of Alloy 600 and Alloy 690: experimentally accelerated study in hydrogenated supercritical water, Metall. Mater. Trans. A (2017) 1–17.

[24] G. Calvarin, R. Molins, A.M. Huntz, Oxidation mechanism of Ni—20Cr foils and its relation to the oxide-scale microstructure, Oxid. Met. 53 (2019) 25–48.

[25] J.-H. Kim, D.-I. Kim, S. Suwas, E. Fleury, K.-W. Yi, Grain-size effects on the high-temperature oxidation of modified 304 austenitic stainless steel, Oxid. Met. 79 (2013) 239–247.

[26] J.-H. Kim, B.K. Kim, D.-I. Kim, P.-P. Choi, D. Raabe, K.-W. Yi, The role of grain boundaries in the initial oxidation behavior of austenitic stainless steel containing alloyed Cu at 700 °C for advanced thermal power plant applications, Corros. Sci. 96 (2015) 52–66.

[27] T.-F. Chen, G. Tiwari, Prasad nbsp, Y. Iijima, K. Yamauchi, Volume and grain boundary diffusion of chromium in Ni-Base Ni-Cr-Fe alloys, Mater. Trans. 44 (2003) 40–46.

[28] S.Y. Persaud, J. Smith, A. Korinek, G.A. Botton, R.C. Newman, High resolution analysis of oxidation in Ni-Fe-Cr alloys after exposure to 315 °C deaerated water with added hydrogen, Corros. Sci. 106 (2016) 236–248.

[29] Y.S. Lim, S.W. Kim, S.S. Hwang, H.P. Kim, C. Jang, Intergranular oxidation of Ni-based Alloy 600 in a simulated PWR primary water environment, Corros. Sci. 108 (2016) 125–133.

[30] G. Bertali, F. Scenini, M.G. Burke, Advanced microstructural characterization of the intergranular oxidation of Alloy 600, Corros. Sci. 100 (2015) 474–483.

[31] G. Bertali, M.G. Burke, F. Scenini, N. Huin, The effect of temperature on the preferential intergranular oxidation susceptibility of alloy 600, Metall. Mater. Trans. A 49 (2018) 1879–1894.

[32] L.E. Thomas, S.M. Bruemmer, High-resolution characterization of intergranular attack and stress corrosion cracking of alloy 600 in high-temperature primary water, Corrosion 56 (2000) 572–587.

[33] M. Sennour, P. Laghoutaris, C. Guerre, R. Molins, Advanced TEM characterization of stress corrosion cracking of Alloy 600 in pressurized water reactor primary water environment, J. Nucl. Mater 393 (2009) 254–266.

[34] Y.S. Lim, H.P. Kim, S.S. Hwang, Microstructural characterization on intergranular stress corrosion cracking of Alloy 600 in PWR primary water environment, J. Nucl. Mater. 440 (2013) 46–54.

[35] S. Lozano-Perez, J.M. Titchmarsh, TEM investigations of intergranular stress corrosion cracking in austenitic alloys in PWR environmental conditions, Mater. High Temp. 20 (2003) 573–579.

[36] S.A. Attanasio, D.S. Morton, Measurement of the Nickel/Nickel oxide transition in Ni-Cr-Fe alloys and updated data and correlations to quantify the effect of aqueous hydrogen on primary Water SCC, 11th Int. Conf. on Environmental Degradation of Materials in Nuclear Power Systems, Stevenson, WA, 2003.

[37] W. Kuang, X. Wu, E.-H. Han, J. Rao, The mechanism of oxide film formation on Alloy 690 in oxygenated high temperature water, Corros. Sci. 53 (2011) 3853–3860.

[38] W. Kuang, X. Wu, E.-H. Han, Influence of dissolved oxygen concentration on the oxide film formed on Alloy 690 in high temperature water, Corros. Sci. 69 (2013) 197–204.

[39] M.-R. He, D.C. Johnson, G.S. Was, I.M. Robertson, The role of grain boundary microchemistry in irradiation-assisted stress corrosion cracking of a Fe-13Cr-15Ni alloy, Acta Mater. 138 (2017) 61–71.

[40] H. Dugdale, D.E.J. Armstrong, E. Tarleton, S.G. Roberts, S. Lozano-Perez, How oxidized grain boundaries fail, Acta Mater. 61 (2013) 4707–4713.

[41] K. Fujii, T. Miura, H. Nishioka, K. Fukuya, Degradation of grain boundary strength by oxidation in alloy 600, 15th Int. Conf. on Environmental Degradation of Materials in Nuclear Power Systems-Water Reactors, Colorado Springs, Colorado, USA, 2011.

[42] A. Stratulat, D.E.J. Armstrong, S.G. Roberts, Micro-mechanical measurement of fracture behaviour of individual grain boundaries in Ni alloy 600 exposed to a pressurized water reactor environment, Corros. Sci. 104 (2016) 9–16.

[43] J. Dohr, E. Tarleton, D. Armstrong, T. Couvant, S. Lozano-Perez, Recent insights in the deformation and fracture of oxidized grain boundaries in austenitic alloys: a synergistic experimental and finite element study, 17th Int. Conf. on Environmental Degradation of Materials in Nuclear Power Systems-Water Reactors, Ottawa, Ontario, Canada, 2015.

[44] T. Couvant, J. Caballero, C. Duhamel, J. Crépin, T. Maeguchi, Calibration of the local IGSCC engineering model for Alloy 600, Proceedings of the 18th International Conference on Environmental Degradation of Materials in Nuclear Power Systems – Water Reactors, Springer International Publishing, Cham, 2018.

[45] W. Kuang, G.S. Was, The effect of grain boundary structure on the intergranular degradation behavior of solution annealed alloy 690 in high temperature, hydrogenated water, Submitted to Acta Materialia, 2019.

[46] E.A. West, G.S. Was, Strain incompatibilities and their role in intergranular cracking of irradiated 316L stainless steel, J. Nucl. Mater. 441 (2013) 623–632.

[47] M. Wehbi, T. Couvant, C. Duhamel, J. Crepin, Oxidation of nickel-base welds 182 and 82 in simulated primary water of pressurised water reactors, Mater. High Temp. 32 (2015) 1–9.

[48] M.D. McMurtrey, B. Cui, I. Robertson, D. Farkas, G.S. Was, Mechanism of dislocation channel-induced irradiation assisted stress corrosion crack initiation in austenitic stainless steel, Curr. Opin. Solid State Mater. Sci. 19 (2015) 305–314.